Science AAAS

Structural Mechanism of Abscisic Acid Binding and Signaling by Dimeric PYR1

Noriyuki Nishimura, *et al.*

Science **326**, 1373 (2009);
DOI: 10.1126/science.1181829

The following resources related to this article are available online at www.sciencemag.org (this information is current as of December 4, 2009):

Updated information and services, including high-resolution figures, can be found in the online version of this article at:
http://www.sciencemag.org/cgi/content/full/326/5958/1373

Supporting Online Material can be found at:
http://www.sciencemag.org/cgi/content/full/1181829/DC1

A list of selected additional articles on the Science Web sites **related to this article** can be found at:
http://www.sciencemag.org/cgi/content/full/326/5958/1373#related-content

This article **cites 34 articles**, 19 of which can be accessed for free:
http://www.sciencemag.org/cgi/content/full/326/5958/1373#otherarticles

This article has been **cited by** 1 articles hosted by HighWire Press; see:
http://www.sciencemag.org/cgi/content/full/326/5958/1373#otherarticles

This article appears in the following **subject collections**:
Botany
http://www.sciencemag.org/cgi/collection/botany

Information about obtaining **reprints** of this article or about obtaining **permission to reproduce this article** in whole or in part can be found at:
http://www.sciencemag.org/about/permissions.dtl

Downloaded from www.sciencemag.org on December 4, 2009

Science (print ISSN 0036-8075; online ISSN 1095-9203) is published weekly, except the last week in December, by the American Association for the Advancement of Science, 1200 New York Avenue NW, Washington, DC 20005. Copyright 2009 by the American Association for the Advancement of Science; all rights reserved. The title *Science* is a registered trademark of AAAS.

tibule of the Sec61 complex, we observed a rodlike density contacting the lateral gate helices 2b and 7; in the lumenal vestibule, we found weak and fragmented density. It has been shown previously that in detergent solution the Sec61 complex can productively engage in polypeptide insertion (*6*, *35*, *36*). Hence, for the gating event preceding insertion, we expect that the signal-anchor sequence in our complex is in contact with the PCC. Thus, the rodlike density in the cytoplasmic vestibule (Fig. 6) may resemble the signal-anchor sequence, the position of which would be consistent with previous cross-link data (*37*).

Consequently, the question arises as to what functional state we observe in our complex. One possibility is that the PCC is in the pre-open state, described for the SecYEG-SecA complex (*18*), in which the lateral gate is partially open but the plug is still occluding the central pore. This appears unlikely because the overall conformation, in particular the lateral gate region, is very different (fig. S7C). It appears more likely that we have captured a post-insertion state with a closed or nearly closed lateral gate region. Consistent with this finding, cross-links between helices 2b and 7 revealed a closed lateral gate after insertion of the nascent peptide chain into the SecYEG complex (*38*).

On the basis of our experimental data, several conclusions concerning cotranslational protein translocation can be drawn (Fig. 6E): (i) Only a single copy of the Sec61 complex is recruited to the nontranslating and also the translating ribosome. (ii) In both the yeast Ssh1 complex and the mammalian Sec61 complex, we observed a nascent polypeptide and/or the signal-anchor sequence accommodated within this single-copy PCC, thus strongly indicating that its central pore serves as the conduit for the nascent polypeptide chain. (iii) The lateral gate of the PCC can be in a closed or nearly closed conformation after insertion of the translocating peptide. (iv) The mode of PCC binding to ribosomes appears to be conserved between species and is maintained in the presence or absence of a signal sequence. (v) The main binding site for the PCC is the universal adaptor site at the ribosomal tunnel exit that is contacted mainly by the cytoplasmic loop L8 of the Sec61 complex, whereas loop L6 is also contacting the emerging nascent polypeptide. The observed mode of Sec61 binding fits well with our previous findings that the universal adaptor site also serves to bind SRP (*22*)—mutually exclusive with the PCC—but is then cleared upon SRP receptor interaction to enable PCC binding (*39*).

References and Notes

1. E. C. Mandon, S. F. Trueman, R. Gilmore, *Curr. Opin. Cell Biol.* **21**, 501 (2009).
2. T. A. Rapoport, *Nature* **450**, 663 (2007).
3. M. Halic, R. Beckmann, *Curr. Opin. Struct. Biol.* **15**, 116 (2005).
4. Z. Cheng, Y. Jiang, E. C. Mandon, R. Gilmore, *J. Cell Biol.* **168**, 67 (2005).
5. R. Beckmann *et al.*, *Science* **278**, 2123 (1997).
6. R. Beckmann *et al.*, *Cell* **107**, 361 (2001).
7. C. Breyton, W. Haase, T. A. Rapoport, W. Kühlbrandt, I. Collinson, *Nature* **418**, 662 (2002).
8. J. F. Menetret *et al.*, *J. Mol. Biol.* **348**, 445 (2005).
9. D. Hanein *et al.*, *Cell* **87**, 721 (1996).
10. J.-F. Ménétret *et al.*, *Mol. Cell* **6**, 1219 (2000).
11. D. G. Morgan, J. F. Menetret, A. Neuhof, T. A. Rapoport, C. W. Akey, *J. Mol. Biol.* **324**, 871 (2002).
12. K. Mitra *et al.*, *Nature* **438**, 318 (2005).
13. B. van den Berg *et al.*, *Nature* **427**, 36 (2004).
14. K. S. Cannon, E. Or, W. M. Clemons Jr., Y. Shibata, T. A. Rapoport, *J. Cell Biol.* **169**, 219 (2005).
15. A. R. Osborne, T. A. Rapoport, *Cell* **129**, 97 (2007).
16. J.-F. Menetret *et al.*, *Mol. Cell* **28**, 1083 (2007).
17. J.-F. Menetret *et al.*, *Structure* **16**, 1126 (2008).
18. J. Zimmer, Y. Nam, T. A. Rapoport, *Nature* **455**, 936 (2008).
19. K. Finke *et al.*, *EMBO J.* **15**, 1482 (1996).
20. A. Prinz, E. Hartmann, K. U. Kalies, *Biol. Chem.* **381**, 1025 (2000).
21. S. Wittke, M. Dünnwald, M. Albertsen, N. Johnsson, *Mol. Biol. Cell* **13**, 2223 (2002).
22. M. Halic *et al.*, *Nature* **427**, 808 (2004).
23. D. T. Ng, J. D. Brown, P. Walter, *J. Cell Biol.* **134**, 269 (1996).
24. Materials and methods are available as supporting material on *Science* Online.
25. D. Karaoglu, D. J. Kelleher, R. Gilmore, *Biochemistry* **40**, 12193 (2001).
26. A. R. Osborne, T. A. Rapoport, B. van den Berg, *Annu. Rev. Cell Dev. Biol.* **21**, 529 (2005).
27. T. L. Yahr, W. T. Wickner, *EMBO J.* **19**, 4393 (2000).
28. F. Duong, *EMBO J.* **22**, 4375 (2003).
29. K. U. Kalies, V. Stokes, E. Hartmann, *Biochim. Biophys. Acta* **1783**, 2375 (2008).
30. Single-letter abbreviations for the amino acid residues are as follows: A, Ala; C, Cys; D, Asp; E, Glu; F, Phe; G, Gly; H, His; I, Ile; K, Lys; L, Leu; M, Met; N, Asn; P, Pro; Q, Gln; R, Arg; S, Ser; T, Thr; V, Val; W, Trp; and Y, Tyr.
31. D. Raden, W. Song, R. Gilmore, *J. Cell Biol.* **150**, 53 (2000).
32. L. G. Trabuco, E. Villa, K. Mitra, J. Frank, K. Schulten, *Structure* **16**, 673 (2008).
33. M. le Maire, P. Champeil, J. V. Moller, *Biochim. Biophys. Acta* **1508**, 86 (2000).
34. T. Tsukazaki *et al.*, *Nature* **455**, 988 (2008).
35. B. Jungnickel, T. A. Rapoport, *Cell* **82**, 261 (1995).
36. W. Mothes, B. Jungnickel, J. Brunner, T. Rapoport, *J. Cell Biol.* **142**, 355 (1998).
37. K. Plath, B. M. Wilkinson, C. J. Stirling, T. A. Rapoport, *Mol. Biol. Cell* **15**, 1 (2003).
38. D. J. du Plessis, G. Berrelkamp, N. Nouwen, A. J. Driessen, *J. Biol. Chem.* **284**, 15805 (2009).
39. M. Halic *et al.*, *Science* **312**, 745 (2006).

40. We thank B. Dobberstein (Zentrum für Molekulare Biologie der Universität Heidelberg, Heidelberg, Germany) for microsomal membranes, B. Brügger (Biochemie-Zentrum der Universität Heidelberg, Heidelberg, Germany) for lipid analysis, and J. Frauenfeld and E. van der Sluis for critical discussions. This research was supported by Deutsche Forschungsgemeinschaft grants SFB594, SFB646 (to R.B. and T.B.), and SFB 740 (to T.M.); Knut and Alice Wallenberg Foundation, Stockholm, Sweden (to S.B.); NIH grants P41-RR05969, R01-GM067887 (to K.S.), and GM35687 (to R.G.); NSF grant PHY0822613 (to K.S.); and the European Union and Senatsverwaltung für Wissenschaft, Forschung und Kultur Berlin (UltraStructureNetwork, Anwenderzentrum). Computer time for MDFF was provided through an NSF Large Resources Allocation Committee grant (MCA93S028). Coordinates of the atomic models and cryo-EM maps have been deposited in the PDB [with accession numbers 2ww9 (active Ssh), 2wwa (inactive Ssh), and 2wwb (mammalian translocon)] and in the 3D-EM database [EMD-1651 (yeast) and EMD-1652 (Mammalia)], respectively.

Supporting Online Material
www.sciencemag.org/cgi/content/full/1178535/DC1
Materials and Methods
Figs. S1 to S7
Tables S1 and S2
References

1 July 2009; accepted 21 October 2009
Published online 29 October 2009;
10.1126/science.1178535
Include this information when citing this paper.

Structural Mechanism of Abscisic Acid Binding and Signaling by Dimeric PYR1

Noriyuki Nishimura,[1]* Kenichi Hitomi,[2,3]* Andrew S. Arvai,[2]* Robert P. Rambo,[3]* Chiharu Hitomi,[2] Sean R. Cutler,[4] Julian I. Schroeder,[1] Elizabeth D. Getzoff[2]†

The phytohormone abscisic acid (ABA) acts in seed dormancy, plant development, drought tolerance, and adaptive responses to environmental stresses. Structural mechanisms mediating ABA receptor recognition and signaling remain unknown but are essential for understanding and manipulating abiotic stress resistance. Here, we report structures of pyrabactin resistance 1 (PYR1), a prototypical PYR/PYR1-like (PYL)/regulatory component of ABA receptor (RCAR) protein that functions in early ABA signaling. The crystallographic structure reveals an α/β helix–grip fold and homodimeric assembly, verified in vivo by coimmunoprecipitation. ABA binding within a large internal cavity switches structural motifs distinguishing ABA-free “open-lid” from ABA-bound “closed-lid” conformations. Small-angle x-ray scattering suggests that ABA signals by converting PYR1 to a more compact, symmetric closed-lid dimer. Site-directed PYR1 mutants designed to disrupt hormone binding lose ABA-triggered interactions with type 2C protein phosphatase partners in planta.

The phytohormone abscisic acid (ABA) plays key regulatory roles in physiological pathways for plant growth and development and enables adaptation to abiotic stresses. In the half century since ABA’s discovery (*1*, *2*), much has been learned about its downstream signaling network (*3*, *4*), yet protein recognition mechanisms for this hormone have remained enigmatic. Recently, a cluster of homologous genes that activate ABA signaling was identified in *Arabidopsis thaliana* by groups using different methods: (i) yeast two-hybrid screening, (ii) chemical genetics, and (iii) coimmunoprecipitation analyses (*5*, *6*). In the presence of ABA, the gene products, designated pyrabactin resistance 1 (PYR1) and PYR1-like (PYL), or regulatory components of ABA receptor (RCAR) down-regulate their binding partners, cluster A type 2C protein phosphatase (PP2C) family members (*7*, *8*). These phosphatases, including ABI1, ABI2, PP2CA, HAB1, and HAB2, are negative regulators of early ABA signaling (*9*–*18*). In addition, OST1/SnRK2.6/SnRK2E SNF1-related protein kinases 2 (SnRK2s) are important mediators of ABA signal transduction (*19*–*22*). PYR/PYL/RCAR family members exhibit functional redundancy in ABA perception, and variations in ABA regulation of their binding to PP2C family members (*5*, *6*). Contrasting hypotheses suggest that ABA either binds to PYR/PYL/RCAR proteins directly or forms a molecular "glue" between these proteins and PP2Cs (*5*, *6*, *23*), similar to auxin's role in joining transport inhibitor response 1 (TIR1)–related and AUX/IAA signaling proteins (*24*). Distinct but overlapping functions of different PYR/PYL/RCAR proteins complicate genetic analysis and mechanistic testing in plants but may enhance flexible regulation of ABA signaling to maximize environmental adaptability of plants.

Plant hormone receptors have evolved from diverse protein families (*25*) and operate by distinct protein-hormone and protein-protein binding interactions. Understanding the mechanism of action of ABA receptor(s) has been controversial and challenging, partly attributable to the absence of a structure for an ABA-bound protein complex. Recent structural studies of hormone-bound auxin and gibberellin receptors identified binding sites, characterized protein assemblies,

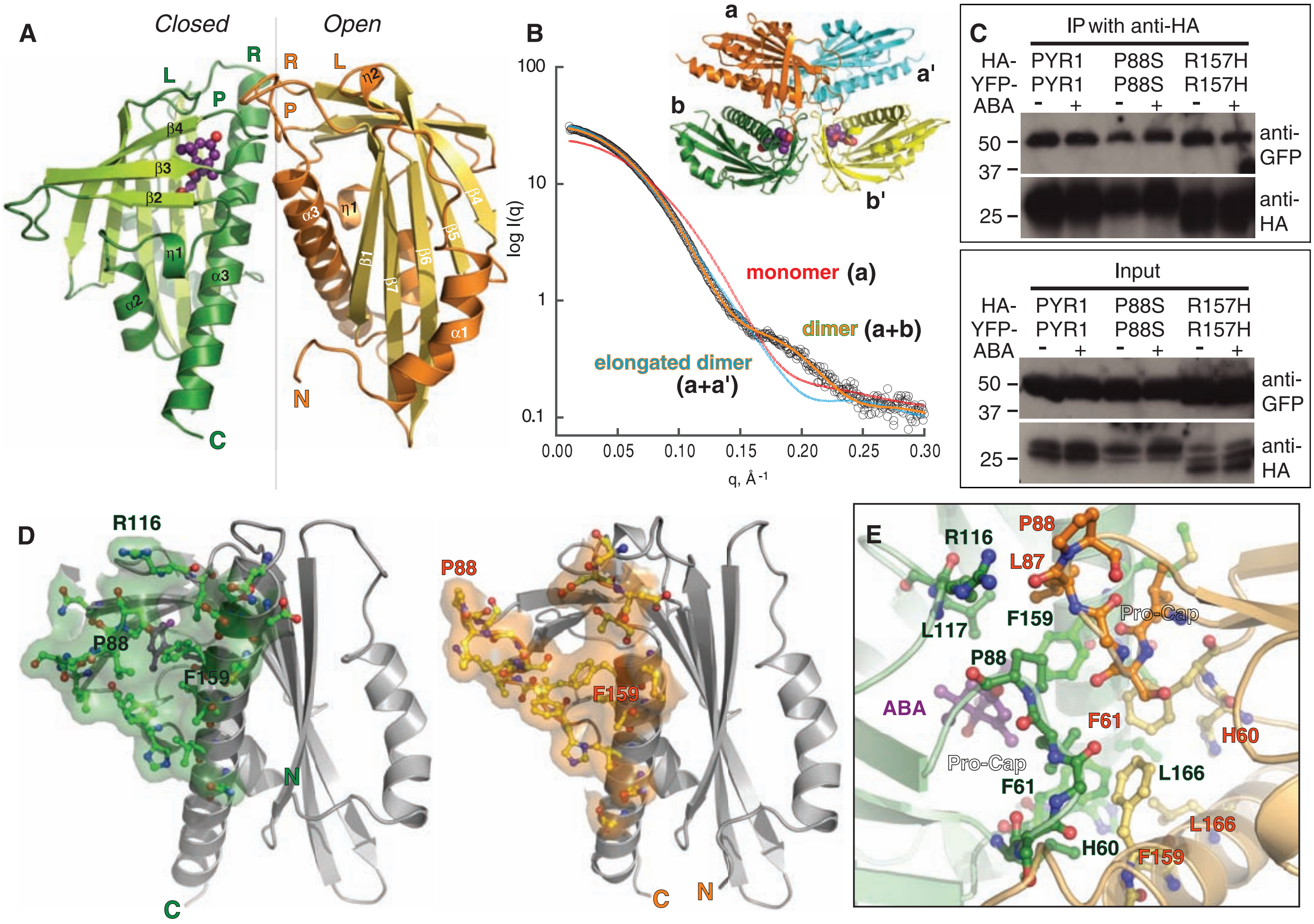

Fig. 1. Dimeric structure of ABA sensor PYR1. (**A**) Crystallographic asymmetric dimer shown as ribbons (labeled β strands and helices) with ABA (purple ball-and-stick model with red oxygen atoms) bound beneath the closed lid of one subunit (left), in a large cavity between the β sheet and long C-terminal α helix. Labeled Pro-Cap (P), Leu-Lock (L), and Recoil (R) structural motifs undergo ABA-induced conformational changes. Vertical line (center) indicates pseudo twofold axis relating the subunits. (**B**) Theoretical SAXS curve (orange line) for asymmetric crystallographic dimer (a+b in inset) matches experimental SAXS data for PYR1 without ABA (open circles), whereas curves calculated assuming a monomer (red) or elongated a+a′ dimer (blue) from crystal lattice (see inset) do not. Curves show the scattering intensity I(q) as a function of the scattering angle 2θ and x-ray wavelength λ, where $q = (4\pi\sin\theta/\lambda)$. (**C**) Coimmunoprecipitation from extracts of plant leaves expressing YFP-tagged PYR1 and HA-tagged PYR1 without (–) and with (+) exogenously applied ABA confirm dimeric PYR1 assembly. After coimmunoprecipitation with an anti-HA matrix, immunoprecipitated (top) and input (bottom) samples were detected with anti–green fluorescent protein (GFP) and anti-HA antibodies. PYR1 wild-type and mutants P88S and R157H are homodimeric in planta, as shown by anti-GFP antibody labeling of YFP-tagged PYR1 coimmunoprecipitated with HA-tagged PYR1. (**D**) Residues and buried surface area contributed to dimer interface by closed-lid (left) and open-lid (right) subunit conformations in asymmetric dimer (*37*). (**E**) PYR1 dimer interface viewed looking down from top in (A) at the interacting lids: open (orange) and closed (green) over ABA (purple). Dimer contacts include the interacting Pro-Cap structural motifs (foreground), plus a side chain–to–main chain hydrogen bond from Arg^{116} in the ABA-bound subunit (top left) to Leu^{87} in the ABA-free subunit.

---

[1]Division of Biological Sciences, Cell and Developmental Biology Section, University of California at San Diego, La Jolla, CA 92093, USA. [2]Department of Molecular Biology and The Skaggs Institute for Chemical Biology, The Scripps Research Institute, La Jolla, CA 92037, USA. [3]Life Sciences Division, Lawrence Berkeley National Laboratory, Berkeley, CA 94720, USA. [4]Department of Botany and Plant Sciences, Center for Plant Cell Biology, University of California at Riverside, Riverside, CA 92521, USA.

*These authors contributed equally to this work.

†To whom correspondence should be addressed. E-mail: edg@scripps.edu

and enabled major advances in understanding hormone signaling in plants (*24*, *26*, *27*). Here, we report the ABA recognition mechanism by the PYR1 dimer assembly, as revealed by ABA-bound and unbound crystallographic structures and small-angle x-ray scattering (SAXS) in solution, coupled with analysis of structure-based, site-directed mutants by coimmunoprecipitation analyses in vivo. Our results show that ABA binds directly to PYR1 within a large internal, water-filled cavity, rather than acting as a molecular glue at an interface with PP2Cs. The PYR1 structure reveals how both (+)-ABA and (–)-ABA enantiomers can show biological activity. We define the unusual asymmetric homodimeric assembly of PYR1 that allows hormone access and sequestration, discover structural motifs (Pro-Cap, Leu-Lock, and Recoil) that mediate "open-" and "closed-lid" conformations, and deduce a probable mechanism for ABA signal transduction via hormone-induced conformational changes that promote binding of PP2C partners.

PYR1 architecture and dimeric assembly. To understand ABA binding and signaling, we crystallized and determined structures (*28*) of *A. thaliana* PYR1 with the phytohormone (+)-*cis*,*trans* abscisic acid [(S-ABA) fig. S1]. Extensive screening produced crystals in space group P2, but only with ABA. Crystallization trials without hormone were unsuccessful, suggesting conformational flexibility. Initial crystals were obtained with enantiomorphic (+/–)-ABA at pH 5.8, the approximate isoelectric point for both protein and hormone. Diffraction quality crystals were reproducible with (+)-ABA alone, at pH values ranging from 5.4 to 6.8, but were always ABA-dependent. Molecular replacement was accomplished with a probe structure from the pathogenesis-related protein Bet vI (Pfam: PF00407) (*29*) family.

The PYR1 structure, determined to 1.7 Å resolution (Fig. 1A, table S1, and movie S1) is a seven-stranded anti-parallel β sheet wrapped around a long C-terminal α helix. This α/β helix–grip fold is shared by plant pollen allergen Bet vI and mammalian steroidogenic acute regulatory lipid transfer (START) proteins (*30*–*32*). The variable N terminus (fig. S2) forms PYR1 helix α1 arching back over the β sheet (Fig. 1A). β1 is hydrogen bonded with β7, but is covalently linked by helices across the β sheet to β2. In contrast, intervening β strands exhibit nearest-neighbor (+1) connectivity. β7 is connected via a projecting loop to C-terminal α3.

In the crystallographic asymmetric unit, PYR1 assembles into a homodimer of one ABA-bound (Fig. 1A, left) and one ABA-free subunit (Fig. 1A, right), related by an ~170° rotation around a pseudo twofold axis. Roughly perpendicular interactions of α3 helices align the β sheets in parallel (Fig. 1A). To determine whether PYR1 (monomer Mr = 20 kD) forms this dimer in solution, we used multiangle laser light scattering (MALS) and SAXS (*33*, *34*). MALS allowed simultaneous measurements of absolute molecular weight and hydrodynamic radius. In the absence of ABA, PYR1 forms a homodimer in solution (Mr = 40.8 ± 0.4 to 40.9 ± 0.3 kD) under varying pH (5.4 to 7.6) and salt conditions (20 mM NaCl and 20 to 100 mM KCl), including those approximating physiological intracellular levels (100 mM K^+, pH 7.6). Thus, ABA is not required for PYR1-PYR1 homodimer formation. SAXS measurements showed that the PYR1 dimer in solution matched the dimer assembly in the crystallographic asymmetric unit, rather than alternative monomeric, dimeric, or tetrameric packing assemblies within the crystal lattice (Fig. 1B and fig. S3). The maximum intramolecular distance ($D_{\max}$ = 68 Å) determined from the SAXS-derived pair-distance distribution function also matched that measured from the crystallographic structure (69.8 Å).

To determine whether PYR1 is homodimeric in planta, we performed *Agrobacterium*-mediated infiltration of *Nicotiana benthamiana* leaves with both yellow fluorescent protein (YFP)– and hemagglutinin (HA)–tagged PYR1, followed by coimmunoprecipitation analyses. PYR1 constitutively formed a dimer in vivo, both in the presence and absence of exogenously applied ABA (Fig. 1C). Thus, the dimer observed in the crystallographic asymmetric unit is evidently a biological unit for PYR1.

In this asymmetric dimer, the interface lies between the crossed α3 helices (Fig. 1A). The roughly triangular surfaces shielded in each subunit are similar but not identical (Fig. 1D). The core of the dimer interface is centered on the asymmetric hydrophobic packing interactions of Phe^{61} and Phe^{159} from both subunits (Fig. 1, D and E), but the dimer packing specificity may depend on interactions (Fig. 1E) of clustered structural motifs that undergo ABA-induced conformational changes (Fig. 1A).

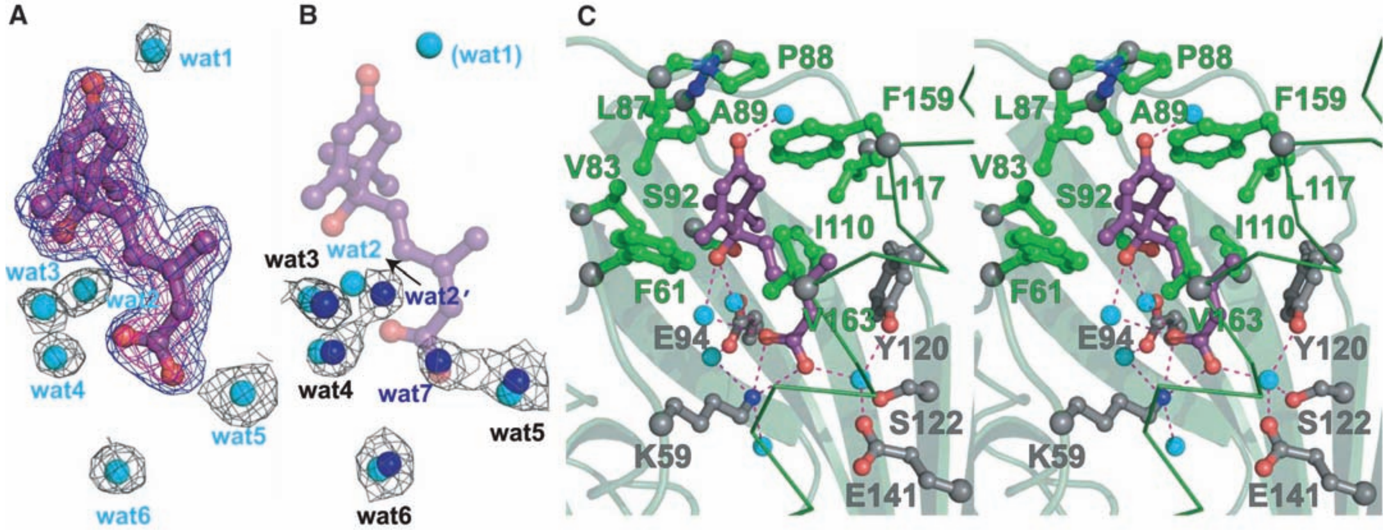

Fig. 2. Water-filled ABA-binding cavity. (**A**) ABA (purple ball-and-stick model, with red oxygen atoms) and adjacent, ordered water molecules (light blue spheres) inside the PYR1 cavity, shown with electron density (mesh). Omit Fo-Fc density for ABA contoured at 3σ (dark blue) and 4σ (magenta); 2Fo-Fc electron density for water molecules contoured at 1σ (black). All maps were calculated after "shaking" coordinates to reduce phase bias. (**B**) Ordered water molecules (dark blue spheres) within the ABA-free subunit cavity, shown with associated 2Fo-Fc electron density, as in (A). ABA (purple) and water molecules (light blue) from the ABA-bound PYR1 subunit [shown in (A)] are superimposed showing conserved water positions. ABA displaces one water molecule (wat7) with the carboxylate, shifts a second (wat2′ to wat2, as shown by arrow), and introduces or stabilizes a third (wat1), which interacts with the ABA carbonyl to stabilize lid closure. (**C**) Stereo view of PYR1 residues contributing to the ABA binding site. Hydrophobic side chains (green ball-and-stick model) surround the ABA ring, whereas hydrogen-bonded (red dashed lines) internal water molecules (light blue spheres) link ABA oxygen atoms (red) to PYR1 hydrophilic side chains (gray ball-and-stick model with red oxygen and blue nitrogen atoms) projecting into the binding cavity. Larger gray spheres show Cα atoms. Lys^{59}, Phe^{61}, Arg^{79}, Val^{83}, Leu^{87}, Pro^{88}, Ala^{89}, Ser^{92}, Glu^{94}, Ile^{110}, Leu^{117}, Tyr^{120}, Ser^{122}, Glu^{141}, Phe^{159}, Val^{163}, and Asn^{167} contribute to forming this large internal cavity.

Abscisic acid binding site inside PYR1. Naturally occurring phytohormone (+)-*cis*,*trans*-ABA, (2Z,4E)-5-[(1S)-1-hydroxy-2,6,6-trimethyl-4-oxocyclohex-2-en-1-yl]-3-methylpenta-2,4-dienoic acid (fig. S1), binds within a large interior cavity of PYR1 between the twisted β sheet and long α3 helix (Fig. 1A). The electron density shows (+)-ABA bound in only one subunit of each PYR1 dimer (Fig. 2, A and B). Hence, the crystal structure resolves both ABA-bound and unbound forms of PYR1. ABA is tethered at both ends by hydrogen bonds to the protein (Fig. 2C). The planar, conjugated, 3-methylpenta-2-*cis*,4-*trans*-dienoic acid tail of ABA extends ~10 Å into a large protein cavity, where the terminal carboxylate is anchored by the inward-pointing Lys^{59} side chain. At the cavity entrance, the ABA carbonyl group links two protein loops via hydrogen bonds with main-chain nitrogen atoms of Ala^{89} and, through a water molecule, Arg^{116}. The adjacent Pro^{88} ring caps the ABA carbonyl to form a lid of the ABA-binding cavity (Fig. 2C); Leu^{87} from the ABA-free subunit reaches across the PYR1 dimer to block the remaining cavity access (Fig. 1E). Thus, PYR1 dimer formation contributes to ABA sequestration.

To biologically test the observed protein-hormone interactions, we made site-directed mutants of PYR1 (fig. S4) designed to weaken ABA binding. To examine their consequences on ABA signaling, these PYR1 mutants were transiently expressed in tobacco leaves, and we analyzed them for function by coimmunoprecipitation assays that detect ABA-triggered interactions between PYR1 and the ABI1 protein phosphatase (Fig. 3). The Lys^{59} → Gln^{59} (K59Q) PYR1 mutation, designed to neutralize the counter-ion to the ABA carboxylate (Figs. 2C and 3A), disrupted exogenous ABA-induced PYR1 binding to ABI1 (Fig. 3B). Thirteen of 14 ABA sensor family members conserve Lys^{59}, whereas PYL13 has Gln (fig. S2). Invariant Arg^{116}, which contributes to both ABA binding and the dimer interface (Fig. 1E), was mutated to Gly. The Arg^{116} → Gly^{116} (R116G) PYR1 mutation also abolished ABA-induced PYR1 binding to ABI1 (Fig. 3B). These mutational results support the biological relevance of the ABA-binding cavity and dimer interface characterized by our crystal structures.

In PYR1, the ABA ring is surrounded by hydrophobic side chains and sequestered from solution (Fig. 2C). This hydrophobic enclosure can accommodate (+)- or (–)-ABA (fig. S1), as shown by our initial 1.8 Å resolution structure determined with mixed enantiomorphic (+/–)-ABA (fig. S5). Within the PYR1 cavity, (–)-ABA maintains the tethering hydrogen bonds and tail position of (+)-ABA. To accommodate the changed chirality, the (–)-ABA ring is flipped ~180° from the (+)-ABA ring (fig. S5), swapping the ring pucker and axial methyl substituent to the opposite side of the cavity. The ring-flipped binding of (–)-ABA provides a structural basis for its varying bioactivity (*35*) in different PYR/PYL/RCAR proteins (*6*). The ABA hydroxyl group, located on the central chiral carbon (figs. S1 and S3), has no protein hydrogen-bonding partner. Instead, two water molecules bridge the ABA hydroxyl and proximal carboxylate with hydrogen bonds (Fig. 2). Another water molecule links the distal ABA carboxylate oxygen to invariant Tyr^{120}, Ser^{122}, and Glu^{141} (Fig. 2C). This complex water-bridged hydrogen-bonding network also interconnects ABA through Glu^{94} to Ser^{92} and Arg^{79} and through Glu^{141} to Asn^{167}. Chemically induced *Arabidopsis* mutants identified by ABA signaling deficiencies (*6*) include PYR1 mutants with inward-facing Glu^{94} and Glu^{141} mutated to Lys (Fig. 3A). The ABA tail is sandwiched between Ile^{110} and Val^{163} (Fig. 2C), and the large internal PYR1 cavity extends beyond this tail. Thus, most structural elements of PYR1 (fig. S2) contribute to ABA-binding cavity formation: helix α3, strands β3 to β7, and loops preceding β2 and joining β3 to β4 and β5 to β6 (Fig. 1A). This architectural design creates the ABA-binding cavity, hydrogen-bonding network, and conserved ordered waters in the absence of ABA, as seen in the ABA-free subunit of the PYR1 dimer (Fig. 2B).

ABA-induced subunit conformational changes. Superposition of ABA-bound and free subunits of the PYR1 dimer (Fig. 4A) revealed substantial conformational differences in three loop motifs. Upon ABA binding, proline cap ("Pro-Cap," Val^{83}-Asn^{90}) and leucine lock ("Leu-Lock," Glu^{114}-Thr^{118}) motifs fold over ABA to close the lid on the cavity (Fig. 4B), and the "Recoil" motif (Met^{147}-Phe^{159}) coils into helix α3, allowing lid closure (Fig. 4). Between open- and closed-lid conformations, Pro^{88} cis-to-trans isomerization switches the direction in which flanking Leu^{87} and Ala^{89} side chains project (Fig. 4B). A hinge motion of the entire Pro-Cap, pivoting at Ile^{84} and Asn^{90}, directs Leu^{87}, Pro^{88}, and Ala^{89} to close over ABA (Fig. 4B). The closed and open Pro-Caps of the two PYR1 subunits directly interact, contributing substantially to the asymmetric dimer interface (Fig. 1, D and E). This interaction suggests why substitution of Pro^{88} with smaller Ser in the Pro^{88} → Ser^{88} (P88S) mutant (Fig. 3A) reduces ABA-induced PYR1 interactions with PP2Cs (*6*).

Similar to the Pro-Cap, the Leu-Lock motif between Glu^{114} and Thr^{118} also undergoes a hinge motion, allowing Leu^{117} to swing inward to lock against the ABA ring (Fig. 4B). When Leu^{117} is locked in, the Arg^{116} side chain projects outward across the dimer interface (Fig. 1, D and E), and the His^{115} ring flips to block solvent access to the methyl substituents of ABA ring carbon C6′ (fig. S1). In the Recoil motif, Arg^{157} interacts with Asp^{155}, capping the N-terminal end of helix α3 in the ABA-free conformation, whereas this helix is N-terminally extended in the ABA-binding form, and Arg^{157} interacts with Glu^{153} or Asp^{161} (Fig. 4B). The Ser^{152} → Leu^{152} (S152L) mutant of PYR1 (Fig. 3B), like the P88S mutant, reduces ABA-induced PYR1 interactions with PP2C (*6*). Some PYR/PYL homologs have Cys at the Arg^{157} position of PYR1 (fig. S2), presumably contributing to structural modulation differently, perhaps by disulfide bond formation with nearby Cys^{30}. Conformational changes in the Pro-Cap, Leu-Lock, and Recoil motifs appear concerted (Fig. 4B):

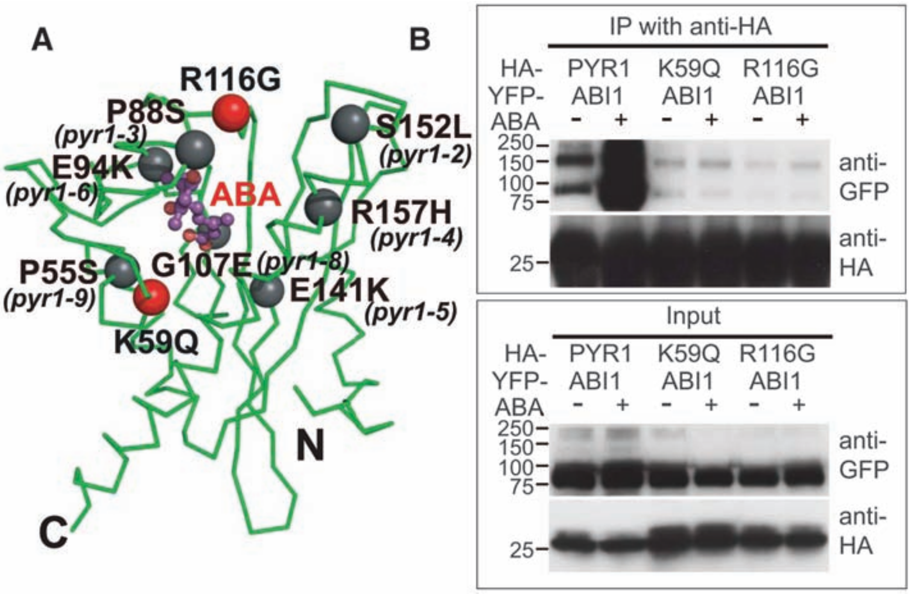

Fig. 3. Disruption of PYR1-ABI1 interactions by single-site PYR1 mutations. (**A**) PYR1 mutants designed from the structure (red) and identified after chemical mutagenesis and screening (gray) (*6*) are mapped to the PYR1 subunit structure (green Cα trace). (**B**) Coimmunoprecipitation from extracts of plant leaves expressing YFP-tagged ABI1 phosphatase with HA-tagged wild-type and mutant PYR1 proteins in planta, both in the absence (–) and presence (+) of exogenously applied ABA. After coimmunoprecipitation by an anti-HA matrix, immunoprecipitated (top) and input (bottom) samples were detected with anti-GFP and anti-HA antibodies (labeled at right). Structure-based PYR1 mutants designed to disrupt ABA binding (K59Q and R116G) folded properly (fig. S5) but lost ABA-induced interactions with ABI1 phosphatase.

Pivoting of invariant Phe^{159} of α3 to pack against ABA probably triggers the Recoil motif to coil back into helix α3, thus allowing lid closure by the Pro-Cap and Leu-Lock motifs (movie S2). Hence, direct interactions of ABA with Phe^{159}, Leu^{117}, and Leu^{87} (Fig. 4B) coordinate interactions of the Recoil, Leu-Lock, and Pro-Cap motifs to complete ABA enclosure.

ABA-induced conformational changes in dimer assembly. ABA-induced conformational changes, monitored by SAXS, render the PYR1 dimer more compact, flatter, and less irregular (Fig. 5). The crystallographic asymmetric dimer, containing one ABA-bound and one ABA-free subunit, produces an excellent fit to PYR1 SAXS curves (Fig. 1B), particularly for data collected in the absence of ABA (χ^2 = 1.2). When excess ABA was added (~four ABA molecules per protein subunit) to the PYR1 dimer in solution, the Guinier radius of gyration decreased (23.71 ± 0.04 to 22.72 ± 0.07 Å), and the pair-distance distribution function describing intramolecular distances became narrower and shifted to shorter distances (Fig. 5A), although the maximum intramolecular distance ($D_{\max}$ = 68 Å) remained constant. SAXS data collected in the presence of ABA were not fit as well (χ^2 = 3.3 to 3.4) by the crystallographic dimer or a dimer modeled with two ABA-bound subunits.

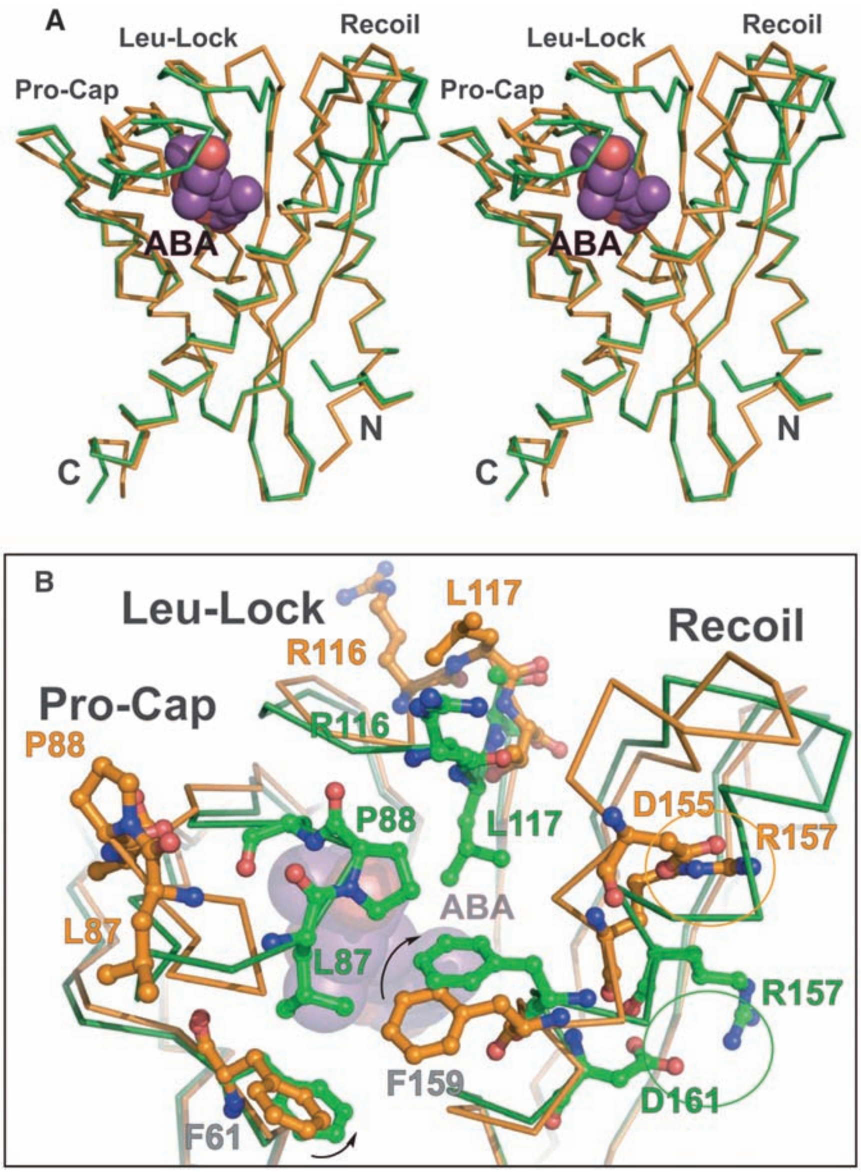

Fig. 4. ABA-induced subunit conformational changes. (**A**) Stereo image showing superposition of ABA-free (orange) and ABA-bound (green) PYR1 Cα traces. ABA-induced helix coiling by the Recoil motif (top right) is coupled to lid closure over ABA (purple with red oxygen atoms) by the Pro-Cap and Leu-Lock structural motifs (top left). (**B**) Enlarged view of ABA-triggered conformational changes in these three structural motifs that close the lid over bound ABA, colored as in (A). ABA (beneath center) triggers rotation of Phe^{159} (arrow) to coil the Recoil motif into helix α3 (diagonal at right), switching the Arg^{157} charge-charge interaction (circled) to a new partner within (rather than outside) this helix. Pro^{88} isomerization from cis (orange, far left) to trans (green, center) converts the open-lid Pro-Cap to the closed-lid conformation, clamping Leu^{87}, Pro^{88}, and Ala^{89} over ABA. Leu^{117} (orange, top center) locks down (green, center) against ABA, closing the Leu-Lock and flipping the preceding Arg^{116} side chain (orange, top center) toward the opposing subunit (forward and slightly to the right in this view) across the dimer interface (see also Fig. 1E).

Ab initio bead models, derived from solution SAXS experiments for PYR1 in the absence of ABA, are asymmetric and match the crystallographically determined dimer (Fig. 5, B to E). In contrast, ab initio models from SAXS experiments for PYR1 with excess ABA are flatter and more compact (Fig. 5, B and C), consistent with a structural model consisting of two ABA-bound PYR1 subunits related by exact twofold symmetry (Fig. 5, D and F). These shapes depict a flattened biconcave disk resembling a red blood cell (Fig. 5, B and F). The twofold symmetry axis and perpendicular direction traversing both subunits of the dimer form ~60 Å disk diameters, whereas the cross-strand width of the β sheet roughly aligns with the ~30 Å disk thickness. In contrast, the ab initio shapes and crystallographic model representing the PYR1 dimer in the absence of ABA depict a more irregular biconcave disk (Fig. 5, B to E), resulting from asymmetric interactions between open- and closed-lid subunit conformations (Fig. 1E and movie S2) and their ~10° deviation from twofold (180°) symmetry (Fig. 5D).

Implications for ABA perception and signaling. The crystal structure, solution SAXS assemblies, and coimmunoprecipitation in vivo provide key insights into molecular and structural mechanisms mediating hormone recognition and signaling by the ABA sensor PYR1. ABA binding inside an occluded protein cavity shows PYR1 to be a direct ABA receptor and signal transduction partner, like the gibberellin receptor GID1 (*26*, *27*), rather than one of two hormone-linked co-receptors, like auxin-linked TIR1 and AUX/IAA (*24*).

The PYR1 dimer crystal structure is unexpectedly asymmetric, revealing structures of both unbound, open-lid and ABA-bound, closed-lid subunit conformations (Fig. 1A). SAXS analyses of PYR1 without ABA confirm an asymmetric dimer in solution (Fig. 1B). At the crystallographic asymmetric dimer interface, the open and closed Pro-Caps pack tightly with each other (Fig. 1E). This arrangement provides open access for ABA and possible allosteric interchange of open- and closed-lid subunits upon hormone binding (movies S1 and S2). Coimmunoprecipitation assays confirm homodimeric PYR1-PYR1 assembly in vivo, both with and without exogenous ABA (Fig. 1C). In solution, SAXS analyses indicate that saturating ABA converts PYR1 into a flatter, more compact dimer, reflecting an orientation change between subunits (Fig. 5). Together, our data support ABA-induced conformational changes producing a twofold symmetric closed-lid dimer. Consistent with these results, two-dimensional nuclear magnetic resonance spectra show a single PYR1 conformer with saturating ABA, but also show multiple conformers without ABA (*6*).

ABA-induced conformational differences in PYR1 subunit structure (Fig. 4) and dimer assembly (Fig. 5) point to a structural mechanism for PYR/PYL/RCAR protein-mediated ABA signal transduction to downstream proteins. The molecular surface of the PYR1 dimer exposes several likely interfaces for ABA-dependent assembly of signalosome complexes with PP2Cs (*5*, *6*, *36*) or other potential partners (Fig. 6). Major ABA-induced subunit conformational changes cluster (Fig. 4) around the interacting lids at the "top" of the asymmetric PYR1 dimer (Figs. 1, A and E, and 6A). Therefore, ABA-induced binding of PP2Cs may occur at interfaces overlapping the closed lids of PYR1. PP2C binding would then favor PYR1 lid closure and decrease the ABA off rate, thus explaining observations that ABA binds more tightly to RCAR1 and PYL5 in the presence of PP2Cs (*5*, *23*). Surfaces of the PYR1 dimer altered by ABA-induced subunit reorientation (Fig. 5D) also provide promising interfaces for signaling to protein partners (Fig. 6).

The phytohormone ABA mediates resistance to abiotic stresses, including drought, salinity, and cold (*3*, *4*). The characterized PYR1 motifs and dimer conformations are key to understanding and future chemical manipulation of phytohormone-induced abiotic stress–resistance responses. The crystallographic structure shows that PYR1 is a direct ABA receptor and sensor, signaling hormone binding within an internal cavity through conformational changes affecting

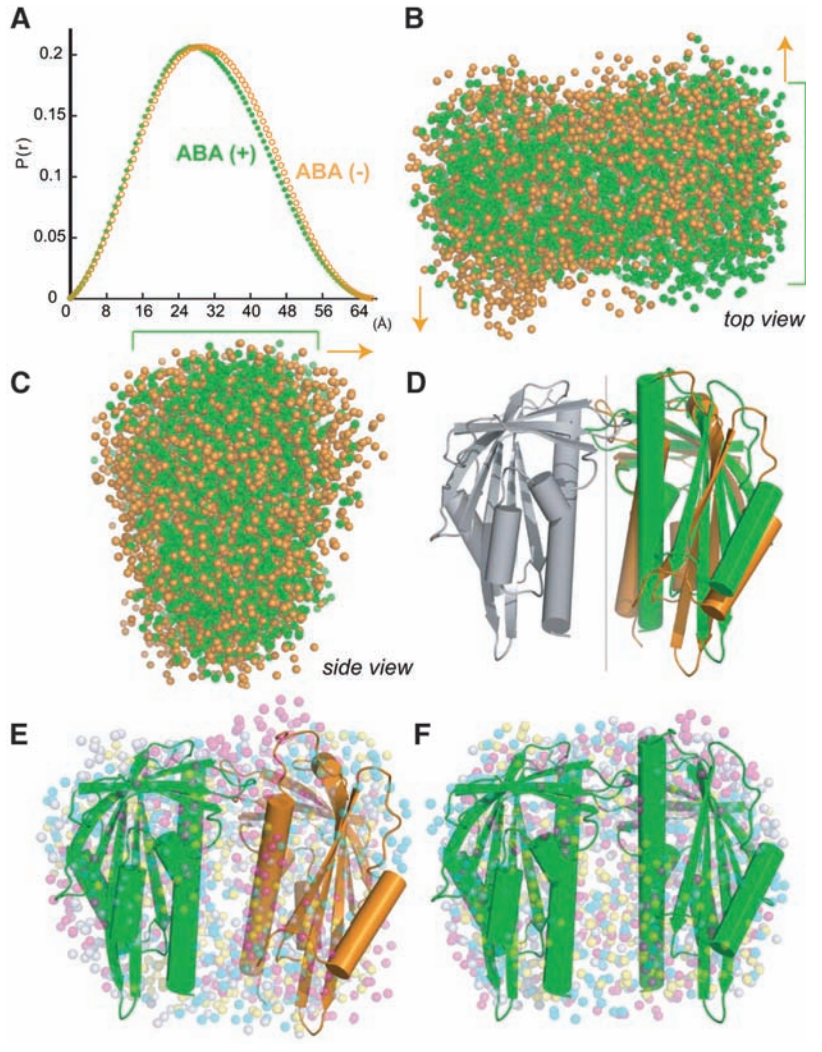

Fig. 5. ABA-induced changes in dimer assembly analyzed by SAXS. (**A**) The pair-distance distribution function describing intramolecular distances in the PYR1 dimer in the absence of ABA (orange) becomes narrower and shifts to shorter distances in the presence of saturating ABA (green). (**B** and **C**) Two sets of eight independent ab initio bead models for the PYR1 dimer, representing SAXS experimental data in the absence (orange) or presence (green) of saturating ABA. Green brackets mark flatter PYR1 disk in the presence of saturating ABA. Orange arrows indicate greater thickness and asymmetry of PYR1 dimer in absence of ABA. ABA-induced changes in subunit orientation make the PYR1 dimer disk flatter and more compact, as seen from top (B) and side (C) relative to orientation in (D). (**D**) Cartoons (depicting α helices as cylinders and β strands as arrows) of the asymmetric crystallographic dimer and a symmetric closed-lid dimer model, aligned by superposition of their common subunit (gray). The ~10° difference in orientation between the second subunits of each dimer (right), highlights the differences between the pseudo twofold axis (~170°) relating subunits (gray and orange) of the asymmetric crystallographic dimer and the exact twofold axis (vertical line) relating subunits (gray and green) of the symmetric dimer model. (**E** and **F**) Independently determined bead models (four sets of colored dots) representing SAXS results in the absence (E) and presence (F) of ABA, each aligned with the corresponding PYR1 structural model (D). The PYR1 dimer assembly shapes determined by SAXS show excellent fits to the crystallographic asymmetric dimer (E) and symmetric dimer model (F). The biconcave, red blood cell shape of the PYR1 dimer is seen by decreased bead density in the center of the PYR1 disks, as well as in the cross section (B), particularly with saturating ABA.

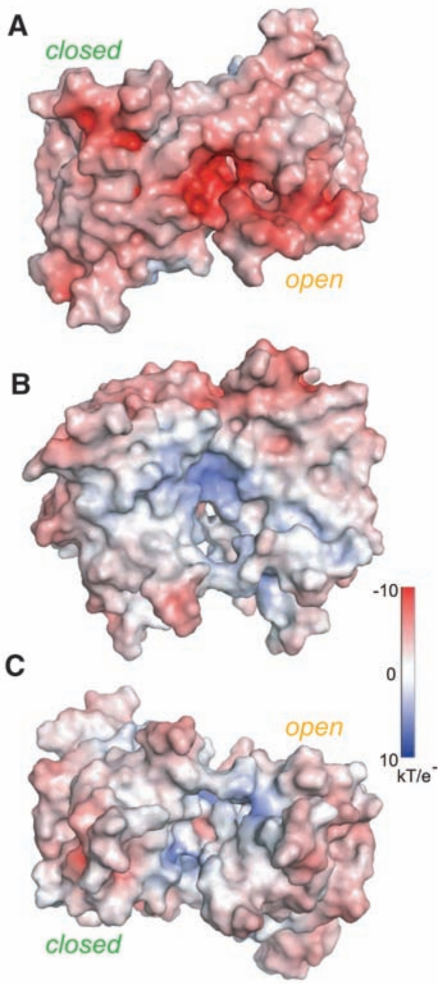

Fig. 6. PYR1 molecular surface color-coded by electrostatic potential. ABA-induced changes in subunit orientation produce conformational changes in the disk-shaped PYR1 dimer at the (**A**) interacting lids (top), (**B**) concave sides, aligned as in Fig. 5, D and E, and (**C**) the cleft (bottom) between C-terminal helices. Conformational changes of charged residues in the Leu-Lock (Glu^{114} and Arg^{116}) and Recoil (Glu^{149}, Glu^{153}, Asp^{154}, Asp^{155}, and Arg^{157}) motifs of each subunit reduce electrostatic surface potential upon lid closure (A).

the dimer interface and assembly. Furthermore, the mechanistic basis of ABA binding reported here provides a framework for future design of alternate ligands for the large ABA-binding cavity to enable chemical activation of abiotic stress resistance in plants.

References and Notes

1. K. Ohkuma, J. L. Lyon, F. T. Addicott, O. E. Smith, *Science* **142**, 1592 (1963).
2. C. F. Eagles, P. F. Wareing, *Nature* **199**, 874 (1963).
3. R. R. Finkelstein, S. S. Gampala, C. D. Rock, *Plant Cell* **14**, S15 (2002).
4. K. Yamaguchi-Shinozaki, K. Shinozaki, *Annu. Rev. Plant Biol.* **57**, 781 (2006).
5. Y. Ma *et al.*, *Science* **324**, 1064 (2009); published online 30 April 2009 (10.1126/science.1172408).
6. S.-Y. Park *et al.*, *Science* **324**, 1068 (2009); published online 30 April 2009 (10.1126/science.1173041).
7. J. Leung *et al.*, *Science* **264**, 1448 (1994).
8. K. Meyer, M. P. Leube, E. Grill, *Science* **264**, 1452 (1994).
9. F. Gosti *et al.*, *Plant Cell* **11**, 1897 (1999).
10. S. Merlot, F. Gosti, D. Guerrier, A. Vavasseur, J. Giraudat, *Plant J.* **25**, 295 (2001).
11. A. Saez *et al.*, *Plant J.* **37**, 354 (2004).
12. N. Leonhardt *et al.*, *Plant Cell* **16**, 596 (2004).
13. G. J. Allen, K. Kuchitsu, S. P. Chu, Y. Murata, J. I. Schroeder, *Plant Cell* **11**, 1785 (1999).
14. Y. Murata, Z. M. Pei, I. C. Mori, J. Schroeder, *Plant Cell* **13**, 2513 (2001).
15. T. Yoshida *et al.*, *Plant Physiol.* **140**, 115 (2006).
16. J. M. Kuhn, A. Boisson-Dernier, M. B. Dizon, M. H. Maktabi, J. I. Schroeder, *Plant Physiol.* **140**, 127 (2006).
17. N. Nishimura *et al.*, *Plant J.* **50**, 935 (2007).
18. S. Rubio *et al.*, *Plant Physiol.* **150**, 1345 (2009).
19. A. C. Mustilli, S. Merlot, A. Vavasseur, F. Fenzi, J. Giraudat, *Plant Cell* **14**, 3089 (2002).
20. R. Yoshida *et al.*, *Plant Cell Physiol.* **43**, 1473 (2002).
21. H. Fujii, P. E. Verslues, J. K. Zhu, *Plant Cell* **19**, 485 (2007).
22. H. Fujii, J. K. Zhu, *Proc. Natl. Acad. Sci. U.S.A.* **106**, 8380 (2009).
23. J. Santiago *et al.*, *Plant J.* **60**, 575 (2009).
24. X. Tan *et al.*, *Nature* **446**, 640 (2007).
25. A. Santner, M. Estelle, *Nature* **459**, 1071 (2009).
26. K. Murase, Y. Hirano, T. P. Sun, T. Hakoshima, *Nature* **456**, 459 (2008).
27. A. Shimada *et al.*, *Nature* **456**, 520 (2008).
28. Materials and methods are available as supporting material on *Science* Online.
29. R. D. Finn *et al.*, *Nucleic Acids Res.* **36**, D281 (2008).
30. L. M. Iyer, E. V. Koonin, L. Aravind, *Proteins* **43**, 134 (2001).
31. M. Gajhede *et al.*, *Nat. Struct. Biol.* **3**, 1040 (1996).
32. Y. Tsujishita, J. H. Hurley, *Nat. Struct. Biol.* **7**, 408 (2000).
33. C. D. Putnam, M. Hammel, G. L. Hura, J. A. Tainer, *Q. Rev. Biophys.* **40**, 191 (2007).
34. G. L. Hura *et al.*, *Nat. Methods* **6**, 606 (2009).
35. E. Sondheimer, E. C. Galson, Y. P. Chang, D. C. Walton, *Science* **174**, 829 (1971).
36. N. Nishimura *et al.*, *Plant J.* published online 26 October 2009 (10.1111/j.1365-313X.2009.04054.x).
37. Single-letter abbreviations for the amino acid residues are as follows: A, Ala; C, Cys; D, Asp; E, Glu; F, Phe; G, Gly; H, His; I, Ile; K, Lys; L, Leu; M, Met; N, Asn; P, Pro; Q, Gln; R, Arg; S, Ser; T, Thr; V, Val; W, Trp; and Y, Tyr.
38. We thank G. Bhabha, J. Christie, M. Hammel, G. L. Hura, D. G. Mendoza-Cozatl, M. E. Pique, D. S. Shin, and J. A. Tainer for discussions, plus the Structurally Integrated BiologY for Life Sciences beamline staff and *Arabidopsis* Biological Resource Center. This research was supported by NIH grants GM060396, ES010337 (J.I.S.), and GM37684 (E.D.G.); NSF grants MCB-0918220 (J.I.S.) and IOS0820508 (S.R.C.); U.S. Department of Energy grants DE-FG02-03ER15449 (J.I.S.) plus DE-AC02-05CH11231 and LBNL-LDRI (R.P.R.); and The Skaggs Institute for Chemical Biology (K.H.). J.I.S. and E.D.G. conceived of the project; E.D.G., J.I.S., K.H., N.N., A.S.A., and R.P.R. designed research; N.N., K.H., A.S.A., R.P.R., and C.H. performed experiments; S.R.C. provided reagents and results before publication; K.H., N.N., A.S.A., R.P.R., J.I.S., and E.D.G. analyzed data; and E.D.G., J.I.S., K.H., and N.N. wrote the paper. Crystallographic coordinates and structure factors are deposited in the Protein Data Bank with accession code 3K3K.

Supporting Online Material
www.sciencemag.org/cgi/content/full/1181829/DC1
Materials and Methods
Figs. S1 to S5
Table S1
References
Movies S1 and S2

11 September 2009; accepted 9 October 2009
Published online 22 October 2009;
10.1126/science.1181829
Include this information when citing this paper.

A Population of Compact Elliptical Galaxies Detected with the Virtual Observatory

Igor Chilingarian,[1,2,3]* Véronique Cayatte,[4] Yves Revaz,[5] Serguei Dodonov,[6] Daniel Durand,[7] Florence Durret,[8,9] Alberto Micol,[10] Eric Slezak[11]

Compact elliptical galaxies are characterized by small sizes and high stellar densities. They are thought to form through tidal stripping of massive progenitors. However, only a handful of them were known, preventing us from understanding the role played by this mechanism in galaxy evolution. We present a population of 21 compact elliptical galaxies gathered with the Virtual Observatory. Follow-up spectroscopy and data mining, using high-resolution images and large databases, show that all the galaxies exhibit old metal-rich stellar populations different from those of dwarf elliptical galaxies of similar masses but similar to those of more massive early-type galaxies, supporting the tidal stripping scenario. Their internal properties are reproduced by numerical simulations, which result in compact, dynamically hot remnants resembling the galaxies in our sample.

Present-day clusters of galaxies host rich populations of dwarf elliptical (dE) and lenticular (dS0) galaxies (*1*) having regular morphology and lacking ongoing star formation and interstellar medium (ISM). These galaxies are thought to form by internal processes, such as supernova feedback to the star formation (*2*), or external agents [ram pressure stripping by hot intergalactic gas (*3*) and/or gravitational harassment (*4*)] acting on gas-rich progenitors. Tidal stripping had not been considered an important mechanism governing galaxy formation until the recent discovery of ultracompact dwarf galaxies (UCDs) (*5*, *6*), that is, very compact stellar systems several times more massive than known globular clusters. However, UCDs [$L \sim 10^7 L_\odot$ (luminosity of the Sun)] are about two orders of magnitude less luminous than bright dEs and, therefore, can be studied in only a handful of nearby galaxy clusters.

Compact elliptical (cE), or M32-like galaxies, which are also thought to form through tidal stripping (*7*), have luminosities [$\sim 10^9 L_\odot$ (*8*–*11*)] similar to those of dEs, whereas their half-light radii ($R_e \sim 0.25$ kpc) are several times smaller, resulting in much higher mean surface brightness ($\langle\mu\rangle_e$) values compared with dEs. These two criteria are easy to formalize and apply to members of nearby galaxy clusters at known distances, hence having a known spatial scale. Ground-based optical telescopes cannot resolve objects the size of 0.25 kpc beyond 50 Mpc. To find them in clusters out to 200 Mpc, thus increasing by a factor of 60 the volume of the nearby universe where cEs remain spatially resolved, it is necessary to use the Hubble Space Telescope (HST).

We created a workflow, that is, an automatic data retrieval and analysis system to search for cE galaxies in large data collections provided by the

---

[1]Observatoire de Paris-Meudon, Laboratoire d'Etude du Rayonnement et de la Matiére en Astrophysique, UMR 8112, 61 Avenue de l'Observatoire, 75014 Paris, France. [2]Sternberg Astronomical Institute, Moscow State University, 13 Universitetsky Prospect, Moscow, 119296, Russia. [3]Observatoire de Paris, VO Paris Data Centre, 61 Avenue de l'Observatoire, 75014 Paris, France. [4]Observatoire de Paris-Meudon, Laboratoire Univers et Théories, UMR 8102, 5 Place Jules Janssen, 92195 Meudon, France. [5]Ecole Polytechnique Fédérale de Lausanne, Laboratory of Astrophysics, 51 Chemin des Maillettes, 1290 Sauverny, Switzerland. [6]Special Astrophysical Observatory, Nizhnij Arkhyz, Zelenchukskij Region, Karachai-Cirkassian Republic, 369167, Russia. [7]National Research Council Canada, Herzberg Institute of Astrophysics, 5071 West Saanich Road, Victoria, BC, V9E 2E7 Canada. [8]CNRS, UMR 7095, Institut d'Astrophysique de Paris, 98 bis, Boulevard Arago, 75014 Paris, France. [9]Université Pierre et Marie Curie Université Paris 06, UMR 7095, Institut d'Astrophysique de Paris, 98 bis, Boulevard Arago, 75014 Paris, France. [10]European Southern Observatory, Karl-Schwarzschild-Strasse 2, 85748 Garching bei München, Germany. [11]University of Nice Sophia Antipolis, CNRS, Observatoire de la Côte d'Azur, BP 4229, 06304 Nice Cedex 4, France.

*To whom correspondence should be addressed. E-mail: igor.chilingarian@obspm.fr